Journal of Computational Physics 376 (2019) 1138–1155

Contents lists available at ScienceDirect

Journal of Computational Physics

www.elsevier.com/locate/jcp

A fluid–structure interaction study of soft robotic swimmer using a fictitious domain/active-strain method

Zhaowu Lin [a], Andrew Hess [a], Zhaosheng Yu [c], Shengqiang Cai [d], Tong Gao [a,b,*]

[a] Department of Mechanical Engineering, Michigan State University, USA
[b] Department of Computational Mathematics, Science and Engineering, Michigan State University, USA
[c] Department of Mechanics, Zhejiang University, PR China
[d] Department of Mechanical and Aerospace Engineering, University of California San Diego, USA

ARTICLE INFO

Article history:
Received 13 February 2018
Received in revised form 1 October 2018
Accepted 8 October 2018
Available online 16 October 2018

Keywords:
Fluid–structure interaction
Fictitious Domain method
Artificial muscle
Swimming

ABSTRACT

Biological swimmers often exhibit rich physics due to the hydrodynamic coupling between the fluid flow and the immersed deforming body. Complexity and nonlinearity of their behaviors have imposed significant challenges in design and analysis of robots that mimick biological swimming motions. Inspired by the recent experimental studies of soft robotic swimmers, we develop a fictitious domain/active strain method to numerically study the swimming motion of thin, light-weight robots composed of smart materials that can actively undergo reversible large deformations (e.g., liquid crystal elastomer). We assume the elastic material to be neo-Hookean, and behave like an artificial "muscle" which, when stimulated, generates a principal stretch of contraction. We adopt an active strain approach to impose contractive strains to drive elastic deformation following a multiplicative decomposition of the deformation gradient tensor. The hydrodynamic coupling between the fluid and the solid is then resolved by using the fictitious domain method where the induced flow field is virtually extended into the solid domain. Pseudo body forces are employed to enforce the interior fictitious fluid motion to be the same as the solid structure dynamics. Using the fictitious domain/active strain method, we perform a series of numerical explorations for soft robotic swimmers with both 2D and 3D geometries. We demonstrate that these robot prototypes can effectively perform undulatory swimming and jet-propulsion when active strains are appropriately distributed on the elastica.

1. Introduction

Soft robotics is an emerging area that draws extensive interests from core areas in materials science and engineering, human health and medicine, applied mathematics, and biomechanics. Largely inspired by the existing biological systems, it stimulates new structural design, and has advantages of simple control, light-weight, miniaturization, and affordable rapid fabrication [1–4]. Compared to the conventional robots that are often made of rigid parts, the soft robots that are made from deformable materials can undergo flexible deformation under actuation, which essentially permits infinite degrees of freedom to facilitate complicated operations. The examples include synthetic stimuli-responsive materials such as hydrogel, shape memory polymers (SMPs), electroactive polymers (EAPs), liquid crystal elastomers (LCEs), polymeric nanocomposites,

* Corresponding author.
E-mail address: gaotong@egr.msu.edu (T. Gao).

https://doi.org/10.1016/j.jcp.2018.10.015
0021-9991/

together with biological tissues such as rat muscle tissue [5]. These so-called smart materials have attracted growing attention because of the intriguing shape or volume recovery properties under different external stimuli, such as electric, magnetic, thermal, chemical, light and pneumatic [6–11].

Designing soft swimming robots that undergo active deformations in a fluid is considerably challenging. First of all, fast swimming motions are typically resultant from a significant amount of momentum exchange between the fluid and solid structures to overcome viscous drag force in the fluid, which require robots to generate rapid and stable structural deformations reversibly. Meanwhile, efficient locomotion of a deformable object requires the employment of specific swimming patterns (or swimming gaits) to take advantage of thrust forces from the resultant fluid drag and wake structures behind [12], which is critical especially in the small or finite Reynolds number regime where the viscous effect is important [13]. To take all the factors into account, the dynamical performances of soft robots with various geometries, material properties, as well as the imposed active control schemes, need to be determined jointly with the induced fluid motions. In addition, dynamic instabilities may occur when light-weight structures move in fluid [14,15], which adds complexities in understanding the control mechanisms of how soft robots perform a stable swimming motion. In general, while various different types of soft robots have been manufactured and tested, it is desired to understand their precise swimming mechanisms, which requires the combination of experimental studies with accurate modeling and simulations in design, analysis, and optimization.

In the past decades, numerous computational methods have been developed to simulate interactions between fluid and moving elastic objects. One example is the so-called boundary conforming method, such as the Arbitrary Lagrangian–Eulerian (ALE) finite element method [16,17] and the space–time finite element method [18]. In these methods, the governing equations of both the fluid and solid phases are solved on one set of mesh that is adapted to the deforming solid objects or geometric boundaries. Although the sharp-interface methods can accurately resolve the complex geometries of moving boundaries, the computation cost is high, especially in 3D. This is because for the strongly coupled fluid–elastic system, additional subiterations between the fluid and solid solvers are necessary in order to achieve better convergence [19,20]. Moreover, frequent re-meshing might be necessary in order to follow boundary movement. When the moving-mesh technique is employed (e.g., ALE method), the associated mesh velocities have to be solved as additional unknowns together with the variables in the fluid and solid phases [16,17]. In addition, unstructured meshes (e.g., triangular, quadrilateral, etc.) are often employed in these methods, which adds complexities in parallelization.

Instead of employing body-fitted meshes, the so-called Cartesian grid methods typically use either separate or non-boundary fitted meshes. This approach simplifies the initial mesh generation and avoids the need for moving and/or adaptive meshing to resolve the changing interface which reduces the overall cost and complexity. For example, the immersed boundary method employs overlaid Eulerian and Lagrangian meshes to solve fluid/elastic structure interactions: The Navier–Stokes (N-S) equations are solved on a fixed Eulerian mesh; while the embedded boundaries are tracked by a set of freely moving Lagrangian points. To account for the no-slip conditions at fluid–solid interfaces, appropriate forcing density terms are added to the N-S equations by using proper interpolations between the solution variables at the fixed grid points in the vicinity of the moving boundary and the nearest Lagrangian points [21–26]. Instead of solving the N-S equations in the fluid phase, both the particle-based methods (e.g., Smoothed Particle Hydrodynamics (SPH) method [27]) and the kinetic methods (e.g., Lattice Boltzmann method (LBM) [28–32]) can be flexibly combined with the immersed boundary method to handle complex geometries, and has become more and more popular in dealing with fluid–structure interactions (FSI).

Inspired by the recent experimental designs [5,33], in this work we numerically study the swimming motion of soft robotic swimmers that perform large reversible elastic deformations driven by the imposed actuation. We assume that the elastic material is hyper-elastic, and can be described by the neo-Hookean constitutive relation that permits finite/large nonlinear deformations. To model the muscle-like behaviors, we adopt an active strain model to distribute contracting strains on soft elastica, which is then coupled with the fictitious domain (FD) method [34,35] to resolve the FSIs. The central idea of the active strain model is based on the multiplicative decomposition where the (total) deformation gradient tensor is split into two parts that represent the sequential contributions from the imposed contractions and the elastic response of the material [36,37]. It is different from the so-called active stress approaches where an additional stress term (different from applied mechanical stress) is introduced into the material model [38]. By appropriately applying contracting strains on elastic plates of different (e.g., square, circular, or bell-like) shapes and rigidities, we show that soft robot prototypes of simple geometries can effectively perform undulatory or jet-propulsion swimming motions. The paper is organized as follows. Section 2 is dedicated to the mathematical model of the active strain approach, as well as its implementation in the FD framework. The numerical simulation results of a 2D beam (undulation) and 3D plates (undulation and jet propulsion) with various geometries are presented in Section 3. Discussions and conclusions are made in Section 4.

2. Mathematical model and numerical method

2.1. Active strain model

To begin with, we seek mathematical models that describe the nonlinear mechanics of soft actuating material. Generally speaking, there are typically two different ways of modelling soft actuating material or so-called artificial muscle. One way is decomposing the total deformation of the material into two parts: elastic deformation caused by mechanical stress and

active deformation/strain caused by other stimuli such as light, electric field, thermal field etc. For example, deformation of hydrogel can be decomposed to the elastic part and swelling part [39]; deformation of liquid crystal elastomer can also be decomposed to the elastic strain and stimuli-induced strain. In experiments, active strain can be easily measured. Without any mechanical load, deformation of a free-standing soft material can be measured as a function of the intensity of external stimuli [40]. Here we employ an active strain approach which applies principal contractions in a manner similar to artificial muscle. To apply actuation the deformation gradient tensor $\mathbf{F}$ is decomposed into an active deformation tensor $\mathbf{F}_a$ and an elastic deformation tensor $\mathbf{F}_e$ following multiplicative decomposition [36,37] such that

$$\mathbf{F} = \mathbf{F}_e \cdot \mathbf{F}_a. \tag{1}$$

Here $\mathbf{F}_a$ is effectively an arbitrary function applied to the reference configuration that can be designed in terms of the desired location, direction, sign and strength. For incompressible solids that are considered here, we apply an incompressible restriction on actuation such that $det(\mathbf{F}) = 1$. For simplicity $\mathbf{F}_a$ can be defined in the principal coordinates and transformed to the desired orientation by a standard solid body rotation coordinate transformation. For an artificial muscle that contracts uniaxially when activated, we define $\mathbf{F}_a = \text{diag}[\lambda_1, \lambda_2, \lambda_3]$ where $\lambda_1 < 1$ represents a principal stretch, and $\lambda_2 = \lambda_3 = \sqrt{\lambda_1^{-1}} > 1$ are the correspondingly strains in the other two directions. With total $\mathbf{F}$ being mapped appropriately, the resultant elastic stress can be calculated through the constitutive relation $\boldsymbol{\tau} = \boldsymbol{\tau}(\mathbf{F}_e) = \boldsymbol{\tau}\left(\mathbf{F} \cdot \mathbf{F}_a^{-1}\right)$ for various different kinds of materials (hyperelastic, viscoelastic, composite, etc.). In this study, we assume the active strain tensor to be either a constant or time-dependent. Nevertheless, it is important to mention that the active strain of real muscle can also depend on its loading condition. Therefore, to better characterize the behaviors of artificial muscles (e.g., electroactive polymer or liquid crystal elastomer) under actuation, systematic experimental measurements are required to obtain the relationship between the active strain tensor and the imposed loading conditions.

Alternatively, another widely used approach is the active stress method where the total stress is decomposed into a mechanical part and an active part, and both of which can induce deformation. For instance, Maxwell stress is usually introduced in the constitutive models of dielectric elastomer [41]. In many cases, the above two methods are mathematically identical, due to the fact that the active deformation introduced here is a first order approximation of nonlinear elasticity, and is independent of mechanical stress. There are also other approaches to implement (soft) actuation without using stress or strain decompositions. For example, to mimick swimming motions of slender flexible swimmers such as sperms or nematodes using the immersed boundary method, active forces are directly added to the right-hand-side of the N-S equation by taking the variational derivative of the discrete elastic energy that is constructed based on the targeted local stretches and curvatures [42,43].

2.2. Fictitious domain method

2.2.1. Formulation

To resolve the FSI of soft robotic swimmers, we implement the above active strain model in a fictitious domain (FD) method proposed by Yu [34], who extended the FD formulation of Glowinski et al. [44] for the rigid particles to the case of flexible bodies. The key idea of the FD method is that the interior of the solid is assumed to be filled with a fictitious fluid that is constrained to move at the same velocity with the solid by a pseudo body force (i.e. Lagrange multiplier). The advantage of the FD method is that the flow fields can be solved efficiently with a fixed Cartesian grid. The reader is referred to [34] for the details on the derivation of the FD formulation and the numerical schemes.

In the following, we briefly introduce the formulation and the numerical schemes of the FD method. Suppose that a deformable body of density ρ_s is immersed in the incompressible Newtonian fluid of viscosity μ and density ρ_f. Let Ω denote the entire computational domain containing both solid and fluid domains, and $P(t)$ represent the solid domain. It is noted that tracking swimming objects in the fixed coordinates requires using a very large computational domain, which makes computation very expensive especially in 3D. Alternatively, here we employ an instantaneous inertial frame Ω that co-moves with the swimmer at a certain reference speed $\mathbf{U}$ [45]. Then the dimensionless FD governing equations in weak form for the incompressible Newtonian fluid in the co-moving relative references as

$$\int_{\Omega} \left(\frac{\partial \mathbf{u}_f}{\partial t} + \hat{\mathbf{u}}_f \cdot \nabla \mathbf{u}_f \right) \cdot \mathbf{v}_f \, \mathrm{d}\mathbf{x} + \int_{\Omega} \left(-p\mathbf{I} + \frac{1}{\mathrm{Re}} (\nabla \mathbf{u}_f)^T \right) : \nabla \mathbf{v}_f \, \mathrm{d}\mathbf{x} = \int_{P} \boldsymbol{\lambda} \cdot \mathbf{v}_f \, \mathrm{d}\mathbf{x}, \tag{2}$$

$$\int_{\Omega} q \nabla \cdot \mathbf{u}_f \, \mathrm{d}\mathbf{x} = \mathbf{0}, \tag{3}$$

where $\hat{\mathbf{u}}_f = \mathbf{u}_f - \mathbf{U}$. The dimensionless governing equations for neo-Hookean solid material ($\boldsymbol{\tau} = G(\mathbf{B} - \mathbf{I})$) are solved in the absolute references as

$$\int_P \left[(\rho_r - 1)\left(\frac{d\mathbf{u}_s}{dt} - Fr\frac{\mathbf{g}}{g}\right)\right]\cdot\mathbf{v}_s d\mathbf{x} + \int_P (\nabla\mathbf{v}_s)^T : [\lambda_0 \ln J\mathbf{I} + G(\mathbf{B}-\mathbf{I})]d\mathbf{x}$$
$$-\int_P (\nabla\mathbf{v}_s)^T : \left(-p\mathbf{I} + \frac{1}{\mathrm{Re}}[\nabla\mathbf{u}_f + (\nabla\mathbf{u}_f)^T]\right)d\mathbf{x} = -\int_P \boldsymbol{\lambda}\cdot\mathbf{v}_s d\mathbf{x}, \tag{4}$$

$$\int_P (\mathbf{u}_f - \mathbf{u}_s)\cdot\boldsymbol{\zeta} d\mathbf{x} = \mathbf{0} \tag{5}$$

Equations (2)–(5) represent the fluid momentum equation, the fluid continuity equation, the solid momentum equation, and the velocity constraint in the solid domain, respectively. In these equations, $\mathbf{u}_f$ is the fluid velocity, $\mathbf{u}_s$ the solid velocity, p the fluid pressure, and λ the pseudo body-force (i.e., the Lagrange multiplier). $\mathbf{v}_f$, $\mathbf{v}_s$, q and $\boldsymbol{\zeta}$ are the corresponding variations, respectively. For the original FD method for the passive deformation model, $\mathbf{B} = \mathbf{F}\cdot\mathbf{F}^T$ is the left Cauchy–Green deformation tensor, here $\mathbf{F}$ being the deformation gradient tensor defined as: $\mathbf{F} = \partial\mathbf{x}/\partial\mathbf{X}$, in which $\mathbf{x}$ and $\mathbf{X}$ are the solid current and reference configurations, respectively. J is the determinant of $\mathbf{F}$, and $J = 1$ for the incompressible solid. In contrast, for the active strain model studied, $\mathbf{B} = \mathbf{F}_e\cdot\mathbf{F}_e^T = (\mathbf{F}\cdot\mathbf{F}_a^{-1})\cdot(\mathbf{F}\cdot\mathbf{F}_a^{-1})^T$, where $\mathbf{F}_e$ is the elastic deformation tensor which causes the elastic stress, and $\mathbf{F}_a$ is an input deformation tensor without generating elastic stress. Also $\mathbf{g}$ denotes the gravitational acceleration. The following characteristic scales are used for the non-dimensionlization scheme: L_c for length, U_c for velocity, L_c/U_c for time, $\rho_f U_c^2$ for pressure p, and $\rho_f U_c^2/L_c$ for Lagrange multiplier $\boldsymbol{\lambda}$. The following dimensionless control parameters are also introduced:

$$\begin{aligned}
\text{Density ratio} &: \rho_r = \frac{\rho_s}{\rho_f}\\
\text{Material parameters} &: \lambda_0 = \frac{\overline{\lambda}_0}{\rho_f U_c^2},\quad G = \frac{\overline{G}}{\rho_f U_c^2}\\
\text{Reynolds number} &: \mathrm{Re} = \frac{\rho_f U_c L_c}{\mu}\\
\text{Froude number} &: Fr = \frac{gL_c}{U_c^2}
\end{aligned} \tag{6}$$

where g is the gravity constant, $\overline{\lambda}_0$ is related to the compressibility property of the material and $\overline{G}$ represents the shear modulus. It should be mentioned that for robotic swimmers, the characteristic velocity is defined as $U_c = f_c L_c$ where a reference actuation frequency is chosen as $f_c = 1$ Hz. In addition, in order to enforce the incompressibility constraint of the solid material, i.e., $J = 1$, we impose a penalty function-like approximation by setting a large enough value for λ_0 ($10^4 \sim 10^5$).

2.2.2. Numerical scheme

The problem (2)–(5) is decomposed into fluid, solid and Lagrange-multiplier sub-problems in a partitioned coupling manner as follows [34]:

1. Fluid sub-problem (for $\mathbf{u}_f^*$ and p)

$$\int_\Omega \left(\frac{\mathbf{u}_f^* - \mathbf{u}_f^n}{\Delta t} + \frac{1}{2}(3\hat{\mathbf{u}}_f^n\cdot\nabla\mathbf{u}_f^n - \hat{\mathbf{u}}_f^{n-1}\cdot\nabla\mathbf{u}_f^{n-1})\right)\cdot\mathbf{v}_f \mathrm{d}\mathbf{x}$$
$$+\int_\Omega \left(-p\mathbf{I} + \frac{(\nabla\mathbf{u}_f^*)^T + (\nabla\mathbf{u}_f^n)^T}{2\mathrm{Re}}\right) : \nabla\mathbf{v}_f \mathrm{d}\mathbf{x} = \int_{P^n} \boldsymbol{\lambda}^n\cdot\mathbf{v}_f \mathrm{d}\mathbf{x}^n, \tag{7}$$

$$\int_\Omega q\nabla\cdot\mathbf{u}_f^* d\mathbf{x} = \mathbf{0}, \tag{8}$$

where the vector Lagrange multiplier $\boldsymbol{\lambda}$ serves as a pseudo body force, and needs to be interpolated from the Lagrangian mesh via a Dirac delta function δ via:

$$\boldsymbol{\lambda}^n(\mathbf{x}) = \int_{P^n} \boldsymbol{\lambda}^n(\mathbf{X})\delta(\mathbf{x}-\mathbf{X})\mathrm{d}\mathbf{X}. \tag{9}$$

In the above the Eulerian and the Lagrangian mesh are denoted by $\mathbf{x}$ and $\mathbf{X}$, respectively. We approximate the delta function as a tri-linear function to transfer the quantities between the unstructured Lagrangian mesh and the uniform Eulerian mesh (with grid size $\Delta x = \Delta y = \Delta z$) [22]

$$\delta(\mathbf{x}-\mathbf{X}) = \frac{1}{\Delta x^3}\phi(\frac{x-X}{\Delta x})\phi(\frac{y-Y}{\Delta x})\phi(\frac{z-Z}{\Delta x}). \tag{10}$$

$$\phi(r) = \begin{cases} 1-|r| & |r| \le 1 \\ 0 & |r| > 1 \end{cases}. \tag{11}$$

This sub-problem is essentially the solution of the N-S equation. An efficient finite-difference-based projection method on a homogeneous half-staggered grid is employed [46]. All spatial derivatives are discretized with the second-order central difference scheme. Here we choose the reference speed $\mathbf{U}$ as the swimmer's COM speed at previous time step, and the computational domain position $\mathbf{x}$ is updated at the end of the fluid sub-problem step as

$$\mathbf{x}^{n+1} = \mathbf{x}^n + \mathbf{U}\Delta t. \tag{12}$$

2. Solid sub-problem (for $\mathbf{x}^{n+1}$)

$$\begin{aligned} &\int_{P_o} \frac{\rho_r \mathbf{x}^{n+1}}{\Delta t^2}\cdot\mathbf{v}_s d\mathbf{X} + \int_{P_0} (\nabla_0 \mathbf{v}_s)^T : \left[\lambda_0 \ln J\mathbf{F}^{-1} + G(\mathbf{F}_a^{-1}(\mathbf{F}_a^{-1})^T\mathbf{F}^T - \mathbf{F}^{-1})\right]^{n+1} d\mathbf{X} \\ &= \int_{P_0}\left[\frac{\rho_r \mathbf{x}^n}{\Delta t^2} + \frac{\mathbf{u}_f^*(\mathbf{x}^n)}{\Delta t} + (\rho_r - 1)\left(\frac{\mathbf{x}^n - \mathbf{x}^{n-1}}{\Delta t^2} + Fr\frac{\mathbf{g}}{g}\right)\right]\cdot\mathbf{v}_s d\mathbf{X} \\ &\quad + \int_{P_0} (\nabla_0 \mathbf{v}_s)^T : \left[(\mathbf{F}^n)^{-1}\cdot\boldsymbol{\sigma}_f^*(\mathbf{x}^n)\right] d\mathbf{X} - \int_{P^n} \boldsymbol{\lambda}^n\cdot\mathbf{v}_s d\mathbf{x}^n, \end{aligned} \tag{13}$$

where $\boldsymbol{\sigma}_f^*(\mathbf{x}^n)$ denotes the viscous stress of the fictitious fluid inside the solid domain. The velocity field $\mathbf{u}_f^*$ is interpolated from the Eulerian mesh via

$$\mathbf{u}_f^*(\mathbf{X}) = \int_\Omega \mathbf{u}_f^*(\mathbf{x})\delta(\mathbf{x}-\mathbf{X})d\mathbf{x}. \tag{14}$$

This sub-problem has been re-formulated to enhance the computational robustness at $\rho_r = 1$ without sacrificing accuracy [34]. A Lagrangian finite element method is used for the solution of this problem. We use the eight-node brick element (i.e., tri-linear interpolant) for the spatial discretization of the solid configuration and the Lagrange multiplier. In equation (13), the penalty function term (involving the material expansion modulus) is integrated using Gaussian rule with only one Gaussian point, and all other terms except the Lagrange multiplier term are integrated with 8 Gaussian points ($2\times2\times2$). The Lagrange multiplier term is integrated using the trapezoidal rule. The resulting non-linear algebraic equations are solved with Newton iterations and the linearized equations in each iteration are solved with the conjugate gradient iterative method. Note that $\mathbf{F}_a$ is a function of the reference configuration and time, and is independent of the current configuration, thus it is not more difficult to derive the Jacobian matrix for the active strain model compared to the original passive deformation model.

3. Lagrange multiplier sub-problem (for $\mathbf{u}_f^{n+1}$ and $\boldsymbol{\lambda}^{n+1}$)

$$\int_\Omega \left(\frac{\mathbf{u}_f^{n+1} - \mathbf{u}_f^*}{\Delta t}\right)\cdot\mathbf{v}_f d\mathbf{x} = \int_{P^n} (\boldsymbol{\lambda}^{n+1} - \boldsymbol{\lambda}^n)\cdot\mathbf{v}_f d\mathbf{x}^n, \tag{15}$$

$$\int_{P^n} \left(\mathbf{u}_f^{n+1} - \frac{\mathbf{x}^{n+1} - \mathbf{x}^n}{\Delta t}\right)\cdot\boldsymbol{\zeta} d\mathbf{x}^n = \mathbf{0}. \tag{16}$$

This sub-problem is solved with the direct-forcing scheme [46,47], instead of the original Uzawa iterations [34]. It has been shown that two schemes produced the same results [47].

2.2.3. Validation

Considering that no benchmark problem for the active strain model is available and the original FD method for the passive deformation model has not been validated with quantitative comparisons, we verify the FD method with two benchmark problems: i) flow-induced vibration of a flexible 2D beam that is attached to the downstream side of a stationary cylinder, and ii) flow-induced flapping motion of a 3D flag.

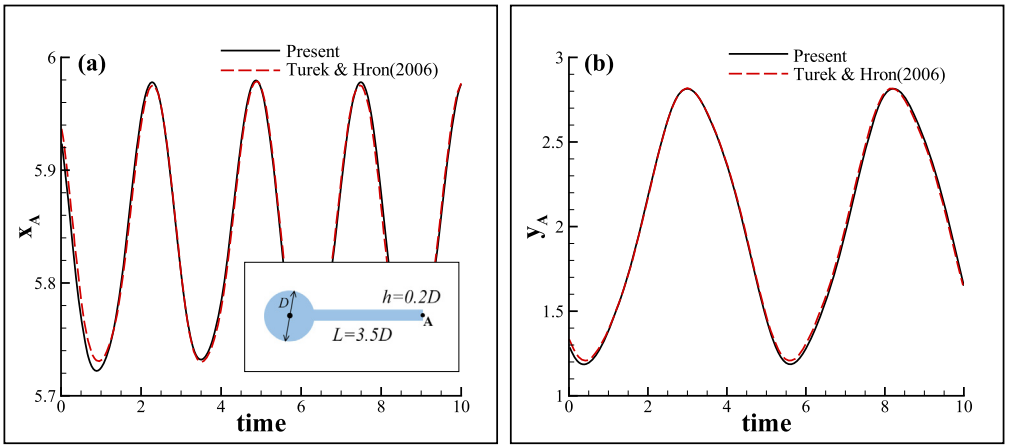

Fig. 1. Time evolution of the displacements in both x- and y-directions of the central point on the plate trailing edge (point A, see inset of (a)) of a thin flexible plate in uniform flow.

Table 1
The amplitude of the central point on the free end and the Strouhal number and the average drag coefficient for a flexible beam.

Works	Amplitude	Strouhal number	Drag coefficient
Turek and Hron (2006) [48]	0.83	0.19	4.13
Tian et al. (2014) [26]	0.78	0.19	4.11
Present	0.81	0.19	4.10

We first consider the case of a 2D flow past a flexible beam that is attached to a rigid cylinder; see inset in Fig. 1(a). The cylinder has a diameter D, and the attached beam has a length $L = 3.5D$ and a thickness $h = 0.2D$. The fluid domain is $L_x \times L_y = 11D \times 4.1D$ We impose are no-slip conditions on the top and bottom, and a far-field condition (i.e., $\partial \mathbf{u}/\partial x = \partial p/\partial x = 0$) on the right boundaries of the computational domain. On the left boundary, we specify a parabolic velocity profile with an average velocity U_0 as: $U(y) = 6U_0 y(L_y - y)/L_y^2$. In this case, we choose $\mathrm{Re} = 100$ by choosing the velocity scale $U_c = U_0$. For elastic material, its rigidity is chosen as $E^* = E/(\rho_f U_0^2) = 1400$. The density ratio between the solid and the fluid phase is chosen as $\rho_s/\rho_f = 10$. The fluid mesh is discretized into uniform grids in both directions with a resolution of 1024×256, while the solid domain is discretized into brick elements with a resolution of 210×12. The time step is chosen as $\Delta t = 0.002$. The time-varying displacements in both directions of the central point on the free end of the beam (point A) is shown in Fig. 1, and is in an excellent agreement with the previous studies. The amplitudes of the y-coordinate of the free end, the Strouhal number and the average drag coefficient ($C_d = \langle F_x \rangle / \left(\frac{1}{2}\rho_f U_0^2 D\right)$) are also summarized in Table 1.

We then consider the second case of a 3D flexible plate of size $(L, h, W) = (1, 0.01, 1)$ in a uniform flow whose leading edge is clamped (h is the plate thickness). The computational domain is rectangular, and its streamwise, transverse and spanwise directions are denoted by X, Y, and Z, respectively. Currently the domain size is chosen as $(L_x, L_y, L_z) = (8L, 8L, 2L)$ based on the plate length L. The uniform velocity U_0 is imposed on the inlet, top and bottom boundaries, respectively. The far-field and periodic conditions are imposed on the outlet and the spanwise direction, respectively. The fluid mesh resolution is $512 \times 512 \times 128$, the number of the solid elements is $80 \times 4 \times 80$, and the time step is $\Delta t = 0.001$. Here we choose Re to be 200, the mass ratio $\rho_s h/\left(\rho_f L\right)$ to be 1.0, the dimensionless bending rigidity $Eh^3/[12(1-\nu_s^2)\rho_f U_0^2 L^3]$ to be 0.0001. The Young's modulus is computed correspondingly for the given plate size and the Poisson's ratio ($\nu_s = 0.4$), and then the shear and volume moduli can be obtained via the relationships $G = E/[2(1+\nu_s)]$ and $\lambda_0 = E/[3(1-2\nu_s)]$. Again, in Fig. 2 and Table 2, our results of both tip displacement and time-averaged drag coefficients show good agreements with the previous studies by Huang and Sung [49], and by Tian et al. [26]. In addition, we have examined the impacts of different interpolating functions on numerical accuracy by choosing either the tri-linear or the smoothed 2-point function [50],

$$\phi(r) = \begin{cases} 3/4 - r^2 & |r| \leq 0.5 \\ 9/8 - 3|r|/2 + r^2/2 & 0.5 < |r| \leq 1.5 \\ 0 & 1.5 < |r| \end{cases}, \tag{17}$$

and found that they indeed yield very similar results.

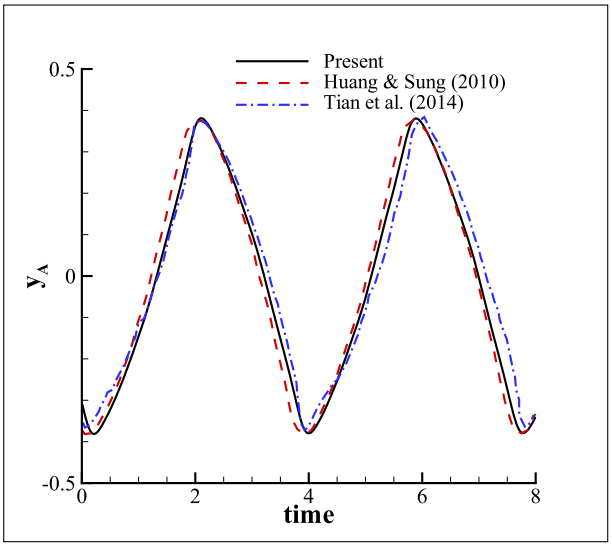

Fig. 2. Time evolution of the transverse displacement of the central point on the plate trailing edge of a thin flexible plate in uniform flow.

Table 2
The amplitude of the central point on the plate trailing edge and the Strouhal number and the average drag coefficient for a flag flapping in uniform flow.

Works	Amplitude	Strouhal number	Drag coefficient
Huang and Sung (2010) [49]	0.780	0.260	
Tian et al. (2014) [26]	0.806	0.266	0.543
Present (tri-linear function)	0.762	0.266	0.579
Present (smoothed 2-point function)	0.760	0.260	0.586

3. Numerical results

Note that slender swimmers (e.g., fish and jellyfish) not only adopt some unique shapes to enhance thrust generation but also distribute muscle inhomogeneously across their thin body to facilitate generation of desired deformation. Therefore, in order for soft robots to achieve effective swimming motions, it is critical to design appropriate swimming strategies (i.e. swimming gaits) by taking into account their geometrical characteristics, material properties, and deformation generation due to the applied active strains. In the following, we show a few successful designs of soft robotic swimmer prototypes that undergo undulatory swimming and jet propulsion by applying active (contracting) strains on different locations of thin elastic plates with different shapes. To seek certain optimized swimming strategies, we systematically explore the parameter spaces by performing direct simulations to resolve the nonlinear fluid/elastic–structure interactions at the moderate Reynolds numbers regime where both the viscous and the inertia forces are important. In all simulations, we fix the density ratio $\rho_r = 1$ for light-weight structures in both 2D and 3D.

3.1. Two-dimensional case

We begin by manipulating a 2D beam of length $L = 1$ and a uniform thickness $h = 0.03$ as shown in Fig. 3(a). Here we consider undulatory motion for slender biological swimmers that perform forward locomotion by generating wavy deformations to produce thrust force. As suggested by the simulation results that use the immersed boundary method [51,52], following the classical Hill muscle model by distributing three-element spring units on the top and bottom surfaces can effectively generate oscillating-switching bending deformations which resemble undulatory swimming motions. Without using complicated models to mimic the biological tissues' mechanical properties (e.g., viscoelasticity, electrophysiology effects [53]), we assume the soft active material is hyperelastic which, at the microscopic level, is driven by a contracting element with a length l and an initial length l_0, yielding an effective contractile strain $\lambda_a = \frac{l}{l_0} = 1 - \lambda_0$ locally. It connects with a neo-Hookean spring that generate elastic stresses in response to the active input of the contraction field which, in 2D, is simply chosen as a homogeneous field $\mathbf{F}_a = \mathrm{diag}\left(\lambda_a, \lambda_a^{-1}\right)$ applied on the active segment δ.

We follow the geometry adopted by Hamlet et al. [51] by choosing the first 10% of body length from the left to be passive, and then connecting an active section of length δ. To activate the beam, as shown in panel (b), we apply the constant ($\lambda_a \sim 1 - \alpha$) or time-dependent (e.g., sinusoidal $\lambda_a \sim 1 - \alpha \sin\left(\frac{2\pi}{T}t\right)$) contractile strain field alternatively on the both sides within a time period T. Here α is an amplitude which characterizes the contraction strength. In the meantime,

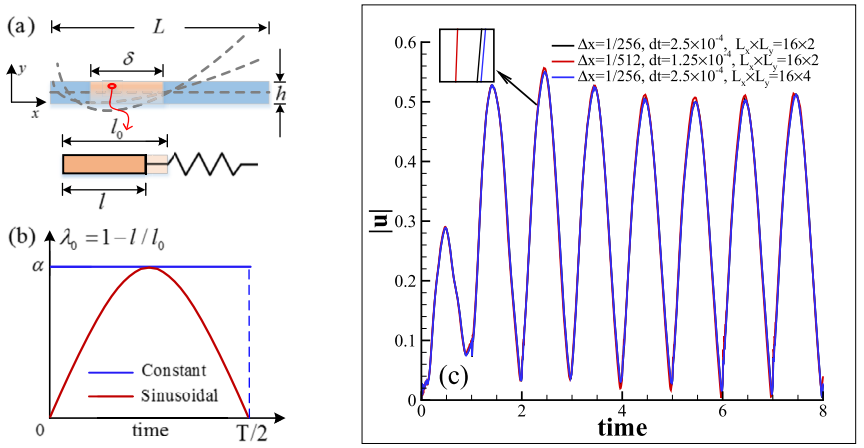

Fig. 3. (a) Schematic of a 2D beam under contracting actuation. The active segment is highlighted in orange. The microscopic mechanical model of the active contraction is illustrated by the zoom-in schematic on bottom. (b) Either a constant (i.e., a step-like) or a sinusoidal contraction is applied during the first half period $0 \le t < T/2$ on the two surfaces alternatively. Then the actuation is turned off for the second half $T/2 \le t < T$. (c) Convergence study for the 2D beam under a sinusoidal actuation by varying domain size, mesh resolution, and time step. The other parameters are $\mathrm{Re} = 500$, $G = 1000$, $\delta = 0.4$, $\alpha = 0.15$, and $T = 2$. (For interpretation of the colors in the figure(s), the reader is referred to the web version of this article.)

the maximum strain is imposed on the surface with an exponential decay in the thickness direction. Mathematically, it is convenient to define λ_a for a constant actuation as

$$\lambda_a = \begin{cases} 1 - \alpha \exp\left(-\frac{h-y}{d_0}\right), & 0 \le \mathrm{t} \le \mathrm{T}/2 \\ 1 - \alpha \exp\left(-\frac{y}{d_0}\right), & \mathrm{T}/2 < \mathrm{t} \le \mathrm{T}. \end{cases} \tag{18}$$

Or,

$$\lambda_a = \begin{cases} 1 - \alpha \sin(\frac{2\pi t}{T}) \exp\left(-\frac{h-y}{d_0}\right), & 0 \le \mathrm{t} \le \mathrm{T}/2, \\ 1 - \alpha \sin(\frac{2\pi t}{T}) \exp\left(-\frac{y}{d_0}\right), & \mathrm{T}/2 < \mathrm{t} \le \mathrm{T} \end{cases} \tag{19}$$

for a sinusoidal actuation. In the above, d_0 controls the steepness of the decay, and is chosen as $h/3$ in all simulations in both 2D and 3D. Typical resultant bending deformations are illustrated in Fig. 3(a) by a few snapshots of the midline position (grey dashed lines). As shown in Fig. 3(c), we have performed a convergence study for the swimming beam under a sinusoidal actuation by varying domain size, mesh resolution, and time step. In the following simulations, we have chosen the Eulerian domain to be $L_x \times L_y = 16 \times 2$, which is uniformly partitioned in the x–y plane with the grid size $\Delta x = 1/256$. The solid domain is partitioned by using rectangular brick elements with the resolution 160×8 so that the area ratio of the Eulerian element to the Lagrangian element is about 1.5 [34].

In Fig. 4, we compare the swimming motions due to different actuation methods (also see movie S1) when choosing $\mathrm{Re} = 500$, $G = 1000$, $\delta = 0.4$, $\alpha = 0.15$, and $T = 2$. Panel (a) shows the magnitude of the instantaneous velocity, i.e., $|\mathbf{u}|$, of the center-of-mass (COM) positions. The spikes suggest sudden changes in the swimming speed due to the way that the actuation abruptly switches between the constant actuation applied two surfaces, while the velocity varies smoothly when the two sides are under a periodic sinusoidal actuation. When projecting the velocity on its swimming direction, the two actuation methods result in approximately the same time-averaged swimming speed $\langle U \rangle \approx 0.13$. In panel (b), we calculate the instantaneous elastic strain energy $E(t) = \int_P w dV$ where $w = \frac{1}{2} G \mathrm{tr}\left(\mathbf{F}_e \cdot \mathbf{F}_e^T - \mathbf{I}\right)$ is the energy density for incompressible materials in terms of the first invariant of the elastic stress tensor [54]. Apparently the sinusoidal actuation requires much gentler elastic deformations compared to the constant one. The snapshots in panels (c) and (d) highlight the drastic differences of the wake structures generated the differing actuation schemes as characterized by the envelop trajectories of the midline (see Inset of panel (b)). As highlighted by the black solid lines in the inset of (b), the beam exhibits larger deformations under a constant actuation. A pair of vortices of opposite sign is generated during each tail upward/downward beating, leading to two vortex streets that are widely separated; see panel (c). In comparison, a sinusoidal actuation yields a smooth swimming motion, shedding vorticies to form a reverse von Kármán vortex street.

Next, we examine the Reynolds number effect by simulating the swimming motions under a sinusoidal actuation when choosing computational parameters $\delta = 0.4$, $\alpha = 0.15$, $T = 1$, $G = 1000$ at $\mathrm{Re} = 100, 500$ respectively. As shown in Fig. 5(a), the swimming plate moves faster as inertia increases even if the elastic deformations at the two Reynolds numbers are similar as shown in panel (b). Panel (c) suggests that at $\mathrm{Re} = 100$, the viscous effect still dominates without significant flow separation and vorticity generation. The undulating deformation is useful to overcome the viscous effect by taking advantage of the anisotropic drag forces exerted upon the beam. As shown in panel (d), apparently the inertial effect at

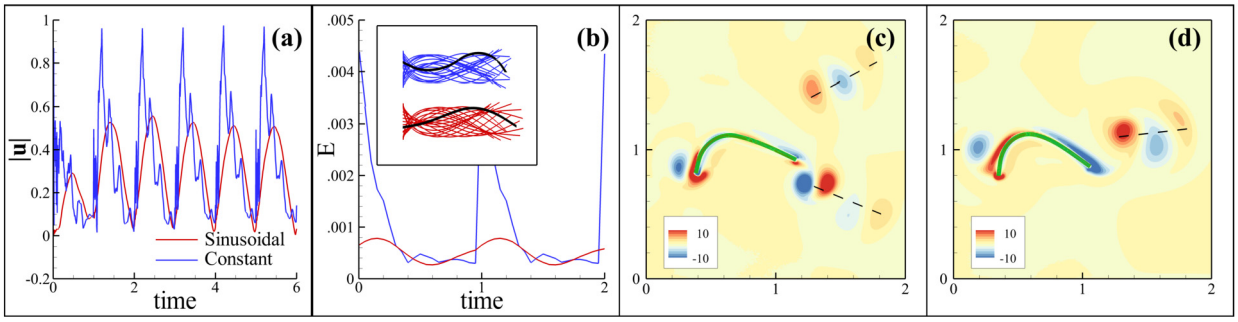

Fig. 4. Swimming motions of a 2D elastic beam under the constant and sinusoidal actuation when fixing $\mathrm{Re} = 500$ and $T = 2.0$. (a) Instantaneous velocity as a function time. (b) Strain energy E as a function of time. Inset in (b): Envelope trajectories of the plate midline during one actuation period. Snapshots of the corresponding vorticity fields are shown in panels (c) (constant) and (d) (sinusoidal).

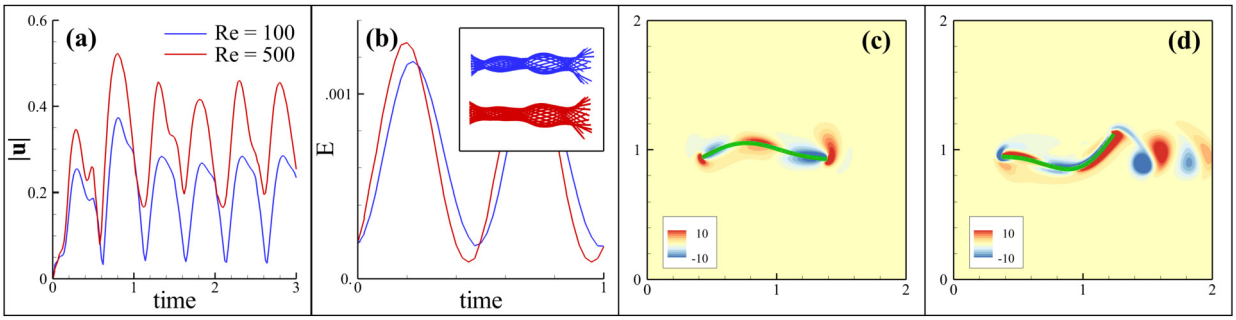

Fig. 5. Comparisons of the free swimming motion of a 2D elastic beam at $\mathrm{Re} = 100$ and $\mathrm{Re} = 500$ when fixing $T = 1.0$ for sinusoidal actuation following Eq. (19). (a) Instantaneous velocities as a function time. (b) Mean elastic energy densities e as a function of time. Inset in (b): Envelope trajectories of the plate midline during one actuation period. Snapshots of the corresponding vorticity fields are shown in panels (c) at $\mathrm{Re} = 100$ and (d) at $\mathrm{Re} = 500$, respectively.

$\mathrm{Re} = 500$ enhances the momentum exchange to generate a reverse von Kármán vortex street, which effectively generates thrust forces to propel the swimmer.

After choosing a particular actuation method (e.g., sinusoidal), we may study the 2D undulating swimming motion by systematically exploring the parameter space of $(\mathrm{Re}, \alpha, T, G, \delta)$. Since simultaneously optimizing all these parameters can be very challenging, here we examine the differences of the 2D swimming motions by varying individual parameters. As shown in Fig. 6(a)–(c), we vary parameter T, G, or δ individually to seek the fastest moving speed $\langle U \rangle$ and maximum swimming efficiency. In panel (a), such motion occurs when $T \approx 1.3$ and the other parameters are fixed. Asymmetric and non-periodic undulations have been observed when actuation is either very fast ($T < 0.5$) or slow ($T > 2.5$), which barely generates a directional motion. In panel (b), when varying G only, the corresponding fastest swimming motion occurs at $G \approx 900$. Interestingly, we have observed that at small G (i.e., $G < 200$), while swimming slowly, the beam in fact can move back and forth as actuation switches sides during one period. When G becomes larger, the beam exhibits a directional motion with its COM velocity sharply increasing before saturating around $U = 0.13$ at $G > 500$. In panel (c), the maximum speed occurs when approximately half of the body is actuated. As δ goes beyond 0.6, we have again observed that non-periodic and asymmetric swimming motions.

In panels (d–f) we estimate the power done by the beam upon the fluid as [55]

$$P = \frac{1}{2}\frac{d}{dt}\int_{\Omega_f} |\mathbf{u}_f|^2 dV + \frac{2}{\mathrm{Re}}\int_{\Omega_f} |\nabla \mathbf{u}_f|^2 dV, \tag{20}$$

based on which we define the swimming efficiency as

$$\eta = \frac{E_k}{E_f + E_k}, \tag{21}$$

where $E_k = \frac{1}{2} M_f \langle U \rangle^2$ is the kinetic energy of the elastic beam, and $E_f = \int_0^T P dt$ represents the total energy delivered to the fluid due to the mechanical work performed by the swimming motion. We have found that P varies approximately monotonically with the varying parameters, leading to the maximum efficiencies around $T = 1.1$, $G = 400$ and $\delta = 0.3$, respectively.

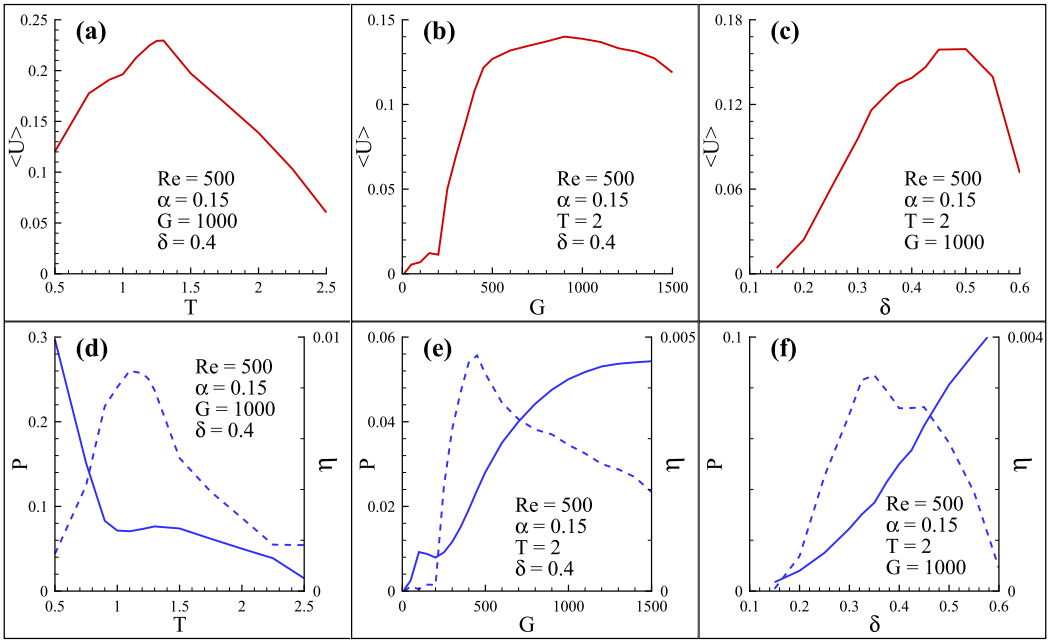

Fig. 6. Measurements of the averaged swimming speed $\langle U \rangle$ in (a–c), and power P (solid blue lines) and efficiency η (dashed blue lines) in (d–f) of an swimming beam under a sinusoidal actuation following Eq. (19) when fixing $\mathrm{Re} = 500$, $\alpha = 0.15$, and varying T, G and δ, respectively.

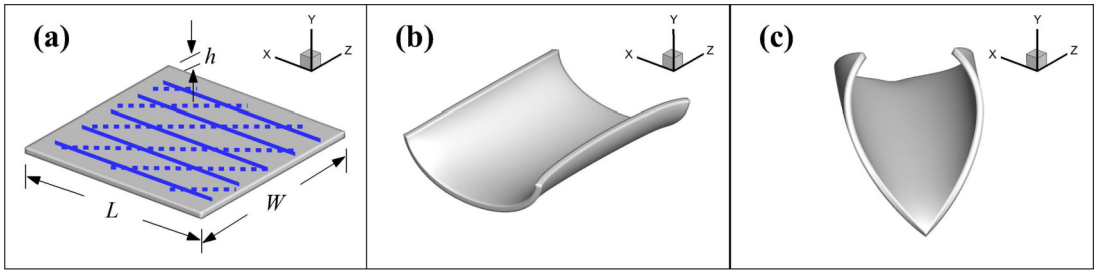

Fig. 7. (a) Examples of different actuation patterns (horizontal vs. diagonal) on the top surface of a square plate, and the corresponding bending deformations in (b) and (c).

3.2. Three-dimensional cases

3.2.1. Deformation control

In 3D, the active strain field can be defined as $\mathbf{F}_a = \mathrm{diag}(\lambda_1, \lambda_2, \lambda_3)$, defined in the principal coordinates in the un-deformed configuration. We align $\lambda_1 = \lambda_a < 1$ with the local contracting direction while defining the remaining principal stretches as $\lambda_2 = \lambda_3 = \lambda_a^{-1/2}$. This assumes that the deformation is homogeneous in the directions of λ_2 and λ_3. However, design and control of elastic deformations in 3D can prove to be much more complicated than in 2D, especially when dealing with complex geometries. As demonstrated in Fig. 7(a)–(c) for a rectangular plate, the resultant bending deformation can be adjusted by distributing the constant contracting field of λ_1 along arbitrary directions (e.g., horizontal in (b) and diagonal in (c)) in the un-deformed configuration.

Another example is shown in Fig. 8, where we change the plate shape from rectangular to circular, and apply a constant actuation in either the radial or the azimuthal direction. Apparently, when radially activated (i.e., $\lambda_a \mathbf{e}_r$, see panel (a)), the plate apparently experiences a two-step deformation during which an intermediate equilibrium shape occurs in panel (b) due to a wrinkling instability, and then relaxes and switches to become a steady-state saddle shape in panel (c). Active deformation involving complex transient dynamics like this is difficult to control, and hence the radial actuation is not preferred. On the other hand, when a constant contraction is applied in the azimuthal direction (i.e., $\lambda_a \mathbf{e}_\theta$, see panel (d)), the circular plate can generate stable reversible bending deformation as shown in panels (e, f). Similar actuation strategies may be used for other thin soft structures with azimuthal symmetry. As shown in Fig. 9, when a radial actuation is applied on the inner surface of an oblate bell (see panel (a)), an opposing expansion occurs in the azimuthal direction due to the material incompressibility, driving a transient wrinkling deformation (see panel (b)). Then the whole body relaxes to become a steady flattened disk as shown in panel (c). Alternatively, as shown in Fig. 8(d–f), applying an azimuthal actuation results

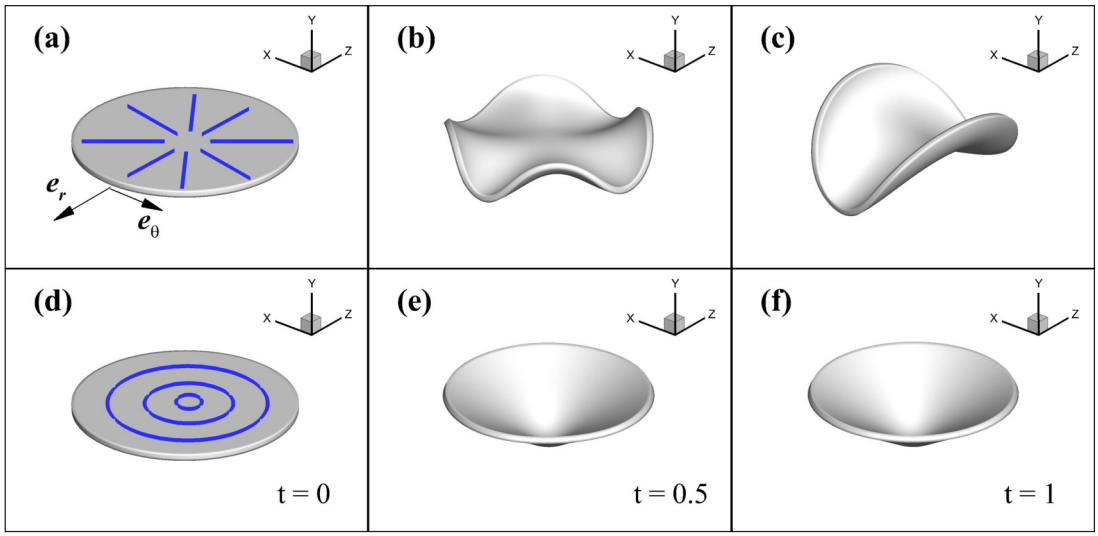

Fig. 8. Snapshots of circular plate under (a–c) radial and (d–e) azimuthal actuation.

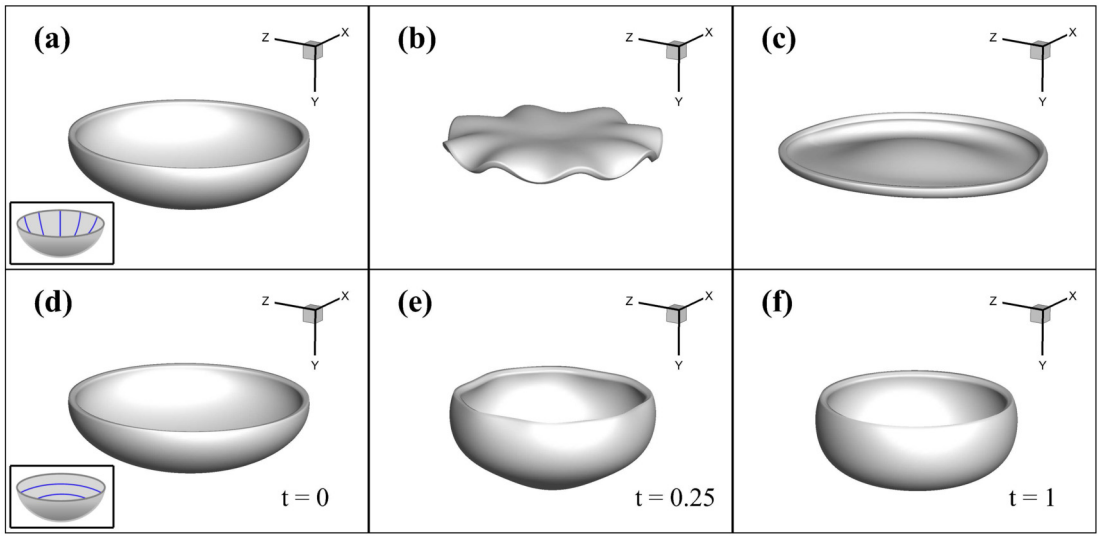

Fig. 9. Snapshots of an oblate bell under (a–c) radial and (d–e) azimuthal actuation.

in efficient contraction of the entire-body, which, as shown below, can effectively be used to generate reversible contraction motions to power a jellyfish robotic swimmer.

3.2.2. Undulation

Similar to the 2D cases discussed in Section 3.1, we first examine the undulatory swimming motion of a 3D rectangular plate. Here we adopt the 2D shape in Fig. 3(a), and extrude the beam of length L and thickness h along its third dimension for a certain width W. In Fig. 10, we show a case of a swimming plate of size $(L, h, W) = (1, 0.03, 0.25)$ that undergoes a quasi-steady undulatory swimming motion, due to sinusoidal contractions (Eq. (19)) applied alternatingly on both sides. Again, a uniform mesh is used for the Eulerian domain $L_x \times L_y \times L_z = 2.8 \times 2.8 \times 0.7$ with the resolution $256 \times 256 \times 64$. The Lagrangian domain $L \times h \times W = 1 \times 0.03 \times 0.25$ is partitioned into brick elements with the solution $84 \times 3 \times 21$, leading to the volume ratio (i.e., Eulerian vs. Lagrangian) about 1.0. The other computation parameters are chosen as $T = 1.0$, $\delta = 0.5$, $G = 1000$ and $\mathrm{Re} = 1000$.

In Fig. 10(a), we visualize the 3D vortex structures by using the so-called λ_{ci} criterion [56,57], together with the distribution of the vorticity component $\omega_z = \frac{\partial u}{\partial y} - \frac{\partial v}{\partial x}$ on a 2D cross-section on the (x-y) plane in panel (b). In contrast to the 2D case where the shedding vorticies form a reverse von Kármán vortex street, here flow separation generates two toroidal structures during each beating motion, leading to two arrays of vortex rings. Apparently, the dynamics quickly become periodic as shown by the COM velocity in panel (c), as well as the strain energy in panel (e), suggesting a quasi-steady free

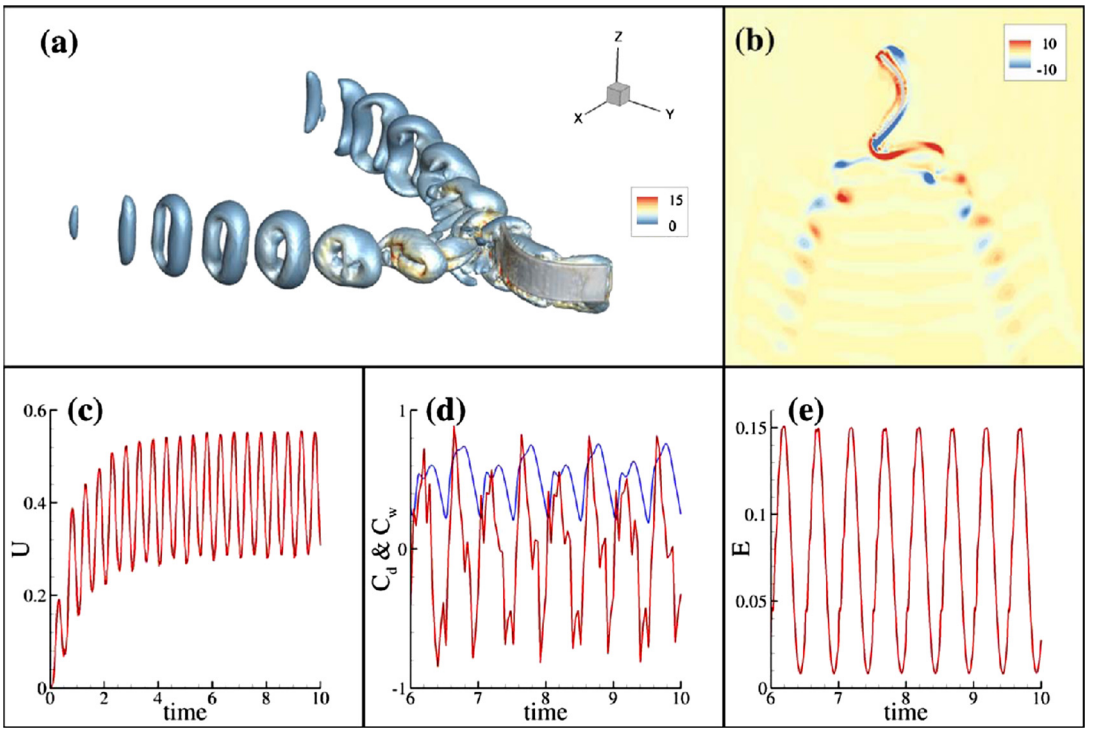

Fig. 10. Snapshots of 3D vortex-core structures (a) and the projection of 2D vortices on the x–y plane (b) of an elastic plate that performs undulation under a sinusoidal actuation following Eq. (19). The computation parameters are chosen as $\alpha = 0.2$, $\delta = 0.5$, $T = 1.0$, $G = 1000$, and $\mathrm{Re} = 1000$. (c) Instantaneous swimming velocity as a function of time. The color bar represents the magnitude of the 3D vorticity, i.e., $|\boldsymbol{\omega}_f|$ (b) Drag coefficient $C_d = F_y / \left(\frac{1}{2}\langle U\rangle^2 A\right)$ (red line) and wake-induced force (i.e., Lamb vector) coefficient $C_w = -F_L / \left(\frac{1}{2}\langle U\rangle^2 A\right)$ (blue line) as functions of time. (e) Strain energy E as a function of time.

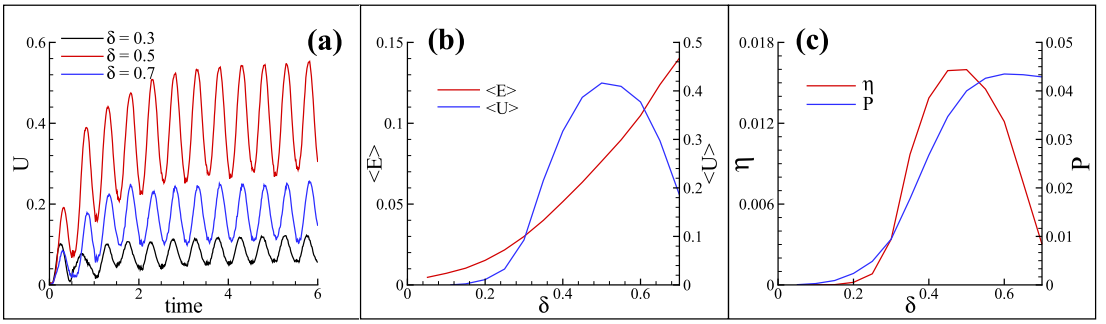

Fig. 11. Simulation results of an undulating swimming motion by varying δ while fixing $\alpha = 0.2$, $T = 1.0$, $G = 1000$ and $\mathrm{Re} = 1000$. (a) Instantaneous swimming speed U at $\delta = 0.3, 0.5, 0.7$, respectively. (b) Time-averaged swimming speed $\langle U\rangle$ and strain energy $\langle E\rangle$ as a function of δ for periodic locomotion. (c) Power P and efficiency η as a function of δ.

swimming motion. In panel (d), we show the drag coefficient $C_d = F_y / \left(\frac{1}{2}\langle U\rangle^2 A\right)$ in the swimming (y) direction, as well as the wake-induced force coefficient $C_w = -F_L / \left(\frac{1}{2}\langle U\rangle^2 A\right)$, where $A = LW$ measures the dimensionless area of plate. Here the drag force is defined by net force exerted on the deformable body. The wake-induced thrust force $\mathbf{F}_L = \int_{\Omega_c} \boldsymbol{\omega}_f \times \mathbf{u}_f dV$ from the vortex structures behind the swimmer, where $\boldsymbol{\omega}_f \times \mathbf{u}_f = \left(\nabla \times \mathbf{u}_f\right) \times \mathbf{u}_f$ is the so-called Lamb vector [58]. We have found that the time-averaged net force is approximately zero, i.e., $\langle C_d\rangle = 0$, since the active strain inputs do not generate extra forces. The oscillations of the $C_d - t$ curve are largely due to the abrupt switches of the actuation on the two sides. In contract, the vortex rings induce negative hydrodynamic forces that vary periodically in the y direction to push fluid backward, which hence contributes to the thrust force generation for the swimming plate.

In Fig. 11 we show an example of varying the active segment length δ using a sinusoidal actuation when choosing $\alpha = 0.2$, $T = 1.0$, $G = 1000$, and $\mathrm{Re} = 1000$. According to the instantaneous swimming velocity U in panel (a), the plate typically starts a steady-steady navigation after performing 5–6 strokes, with a significant increase in the speed when δ goes beyond 0.3. In panel (b), it is observed that the time-averaged swimming speed U increases with δ, and reaches a maximum value when $\delta \approx 0.5$. The time-averaged strain energy $\langle E\rangle$ grows monotonically as δ increases, driven by more

inputs from the contracting strain field through $\mathbf{F}_a$. In panel (c), compared to the 2D case where the swimming power P grows monotonically with δ, it approximately saturates around $\delta = 0.6$, leading to the maximum efficiency at $\delta \approx 0.5$.

3.2.3. Jet-propulsion

Next we examine jet-propulsion based swimming (e.g., jellyfish) that propels the swimmer by squirting out water from the muscular cavity through periodic contractions. We follow the design reported in previous studies [59–62,75] to construct an oblate 3D bell with its initial shape a partial prolate ellipse which can be described as

$$\left(\frac{x}{R_1}\right)^2 + \left(\frac{y}{R_2}\right)^2 + \left(\frac{z}{R_3}\right)^2 = 1 \tag{22}$$

where $R_1 = R_3 = 0.5$ and $R_2 = 0.25$, with a thickness $h = 0.03$. As discussed in Section 3.2.1, in order to generate robust whole-body contractions for a thin circular or bell-like plate, it is preferred to apply an active strain field with the principal contraction occurring in the azimuthal direction to avoid complex transient dynamics and instabilities of thin structures. We employ the same strategy here to apply the active contractions on the outer region of the inner surface marked by the blue circles in the inset of Fig. 12(a). The active segment is taken approximately 1/3 of the total arm-length of the bell. In addition, we thicken the bell top (denoted by ε, and we fix $\varepsilon = 0.1$) in order to stabilize the elastic deformation [63,64], which is important when both α and Re are large.

We employ a constant contraction following Eq. (18), instead of a gentle sinusoidal one which is ineffective in generating rapid deformations as required by jet propulsion. We choose parameters based on the *in vivo* measurements of jellyfish tissue (e.g., mesoglea) [65]. By using the Young's modulus $\overline{G} \approx 100Pa$ (the experimental data are approximately between $10Pa$ and $100Pa$) as well as choosing the characteristic length $L_c \approx 1cm$ [5] and velocity $U_c \approx 1cm/s$, we choose the estimated the range of the dimensionless parameters as $G = 10 \sim 100$ and $\mathrm{Re} = 10 \sim 1000$. An example of jet-propulsion is shown in Fig. 12. The periodic axisymmetric contractions of the oblate elastic bell is reminiscent of the "rowing" motion of a jellyfish [66–68]. As shown in panel (a) for the 3D vortex cores overlaid on the solid mesh, after the initial transient, the elastic bell quickly starts to perform a stable forward swimming motion as the bell arm paddles, leaving behind toroidal vortices [69,70,62,64]. The typical vortex dynamics during one period are illustrated in sequential snapshots of a 2D cross section shown in panels (b–i). In the power stroke corresponding to the first half-period ($0 < t < T/2$, see panels (b–e)), the applied active strains drive an inward contracting deformation. A shear-induced starting vortex is generated at the bell tip, interacting with the stopping vortex from the previous recovery stroke. After the starting vortex pair is separated from the bell arm, it is quickly advected with the jet flow due to the entrained fluid mass that is ejected downward (panels (c–e)). In the 2D plane, it is visualized as a vortex dipole. In the next half-period ($T/2 < t < T$, see panels (f–i)), turning off the active strains relaxes the elastic bell, driving a recovery stroke during which the fluid mass refills the bell. In the meantime, a stopping vortex with an opposite sign is generated and then adhered on the bell tip in the expansion process.

Details of the bell kinematics during one period is shown in Fig. 13. In panel (a), the sequential snapshots of the swimmer's contour are plotted. Note that while actively interacting with the fluid flows, imposing a large step-like contracting deformation of thin soft structures may trigger resonances during which the entire body oscillates quickly. For example, the bell top bounces back and force during contraction (also see Fig. 12(b–e) as well as movie S2), and then overshoots the equilibrium position and swings back during relaxation. Such oscillatory behaviors can be quantitatively characterized by examining the variation of the total strain energy as a function of time in panel (b) where small amplitudes fluctuations are observed, immediately after the active strains being turned on and off. This is also reflected on the instantaneous average velocity in panel (c). As the bell starts to contract, its COM velocity quickly reaches a maximum, and then relaxes following the structural oscillations.

Systematically varying α and Re reveals various different regimes of jellyfish-like swimming motion as a result of the complex fluid–thin structure interactions. The dynamic behaviors are summarized in the phase diagram in Fig. 14(a) where the background colors represent the time-averaged COM velocities at steady state. As explained above, in the regime of large α and Re, the bell exhibits a fast forward swimming motion (see COM velocity marked by the red line in panel (b)), due to the strong positive feedbacks obtained from the fast fluid jet that carries fluid momentum backward. In the regime of smaller α and lower Re, however, while the bell arms are rowing, the locomotion is significantly weakened, largely due to the reduced amount of inputs from active contractions which hence leads to much weaker elastic deformations. Therefore, we find that the contracting deformation and the induced whole-body vibration are comparable. Their interplay eventually leads to complex arm kinematics as well as the momentum exchange between the fluid and the solid phase. Interestingly, we have observed that while swimming slowly (see the COM velocities marked by the blue and black colors in panel (b)), the bell can exhibit both forward (marked by solid squares) and backward (marked by black triangles, see movie S3) movement.

4. Discussion and conclusion

In this work we have developed a FD-based computational framework to simulate swimming motion of soft robots by distributing active contractions on the elastic solid body. The active strain model is based on the multiplicative decomposition of the deformation gradient tensor. As a first order approximation, the induced active deformation is independent

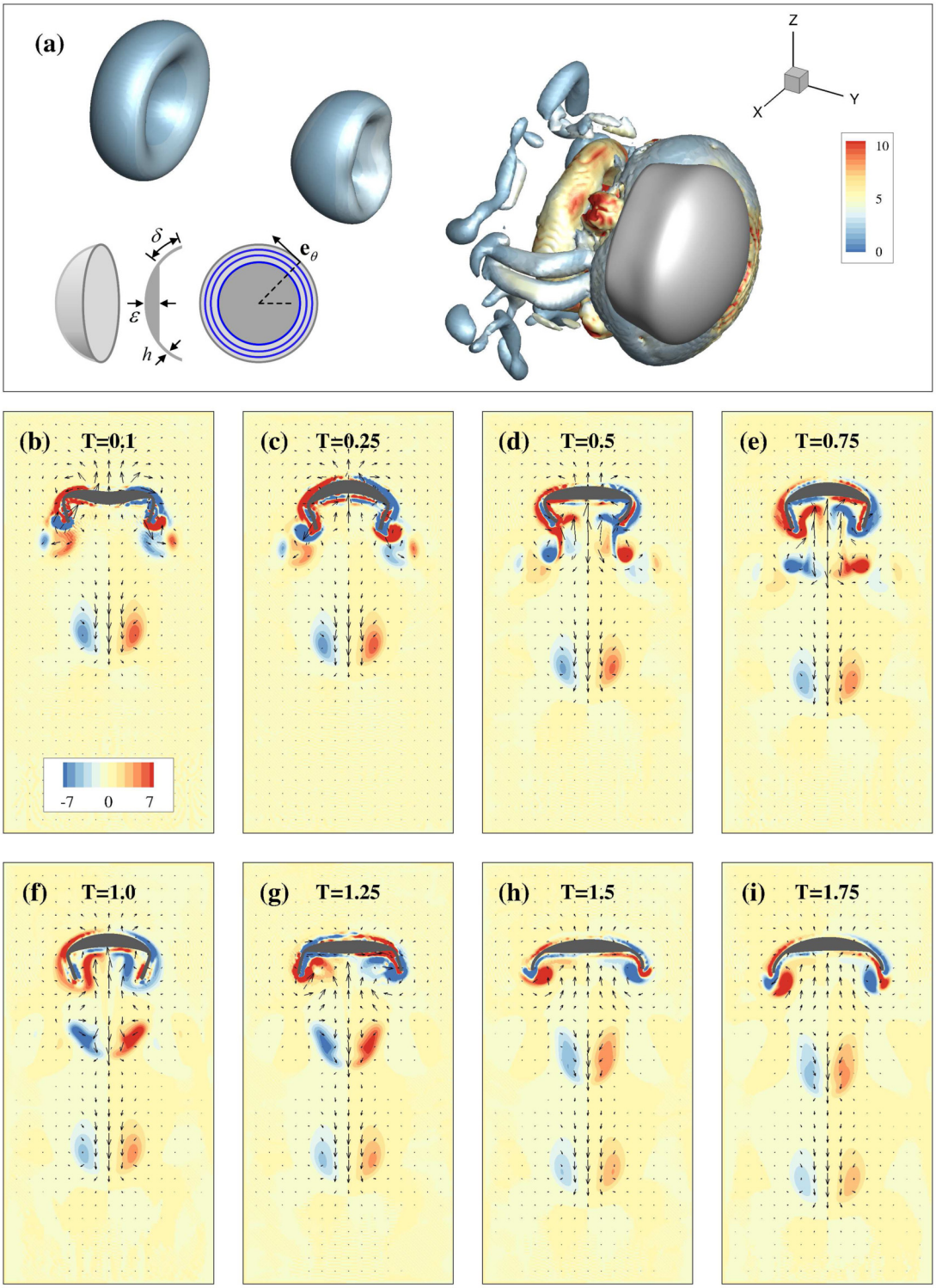

Fig. 12. Typical vortex structures of an elastic bell undergoing jellyfish-like swimming in the moving coordinates, when choosing $\alpha = 0.8$, $T = 2.0$, $G = 100$, $\mathrm{Re} = 500$, $\varepsilon = 0.1$, $\delta = 0.21$, and $h = 0.03$. (a) Vortex core overlaid on the solid mesh. The color bar represents the magnitude of the 3D vorticity, i.e., $|\boldsymbol{\omega}_f|$. Inset: Schematic of the swimming elastic bell with a thickened top and azimuthal actuation. (b–i) In-plane fluid velocity vector field (u, v) overlaid on the colormap of vorticity on a 2D cross section plane during one period.

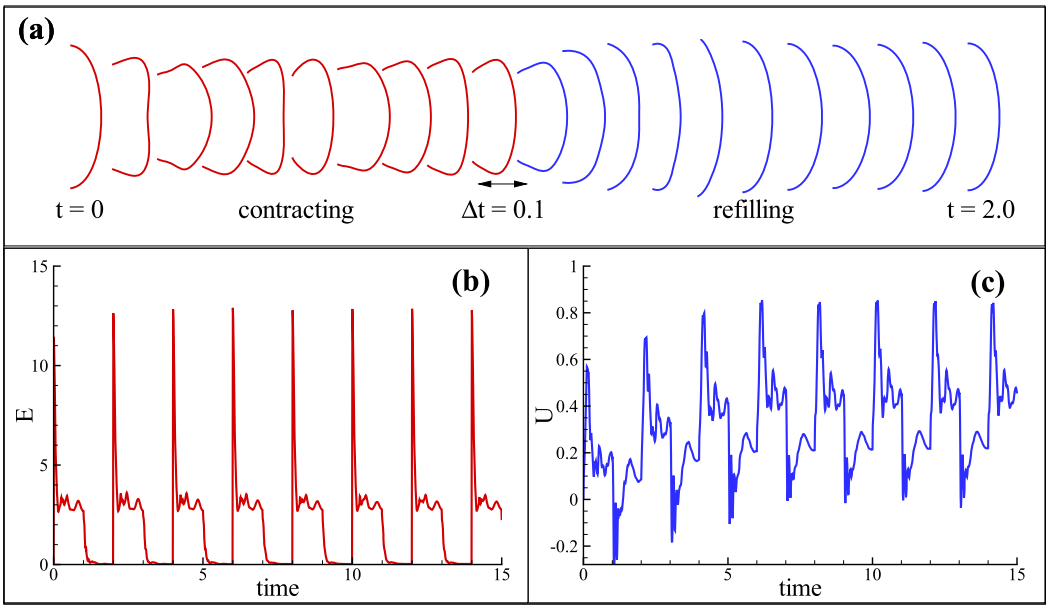

Fig. 13. Highlights of bell's rowing motion accompanying whole-body vibrations through the kinematics of the bell arm during the contracting and refilling process (a). The instantaneous strain energy (b) and COM velocity(c) as function of time.

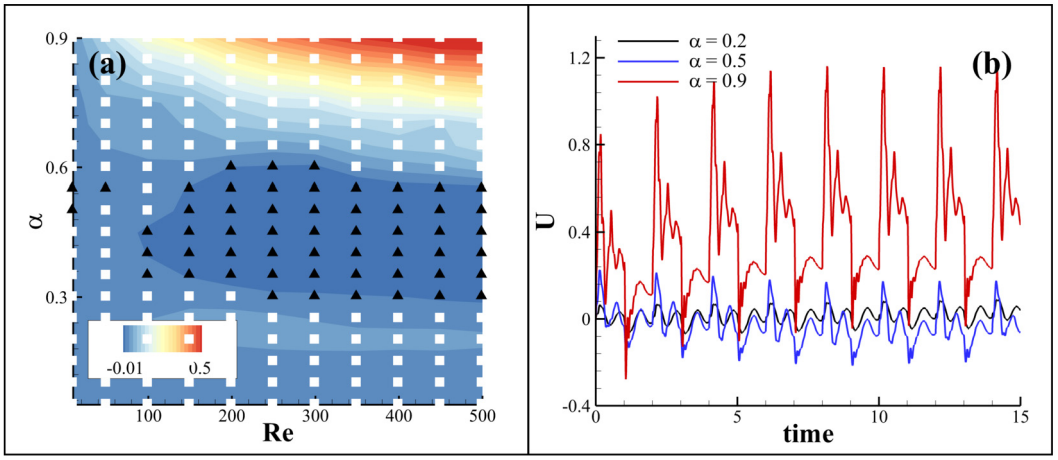

Fig. 14. (a) Phase diagram of (α, Re) for a swimming bell undergoing jet-propulsion locomotion. The while and black symbols represent the forward and backward locomotion, respectively. The background color represents the time-averaged steady-state swimming velocity $\langle U \rangle$ at late times. (b) Typical instantaneous COM velocities when choosing $\alpha's$ in different regimes at $\mathrm{Re} = 250$.

of mechanical stress, and can be easily measured experimentally by varying the external stimuli without imposing any mechanical load. From the biomimetic perspective, the active strain approach makes it straightforward to distribute active contractions in the muscle-fiber directions by following biological muscle architectures. Moreover, it is useful to take advantage of finite thickness of thin elastic structures by imposing an inhomogeneous contraction field to achieve desired elastic deformation.

Using the FD/active-strain method, we have been able to virtually design 2D/3D thin, light-weight soft robots with simple geometries (e.g., square, circle, bell) that perform biomimetic undulation and jet-propulsion. It is also straightforward to activate soft swimmers with more complex geometries by distributing active strains on desired locations. As shown in Fig. 15 and movie S4, we have followed the design by Nawroth et al. [5] to simulate a baby jellyfish (e.g. early-stage Ephyrae) that has a circular-disk body and multiple attached "arms". In particular, it is important to apply strains to follow the jellyfish muscle architecture. As shown in Fig. 15(a), we make the contractions occur in the radial direction to be aligned with the arms, together with a layer of contraction simultaneously imposed in the azimuthal direction near the rim of the circular disk, which turns out to be critical in stabilizing the thin-structure deformation in forward swimming. A typical failure case is shown in Fig. 15(b) (also see movie S4) where only the radial contractions are applied. It is seen that the

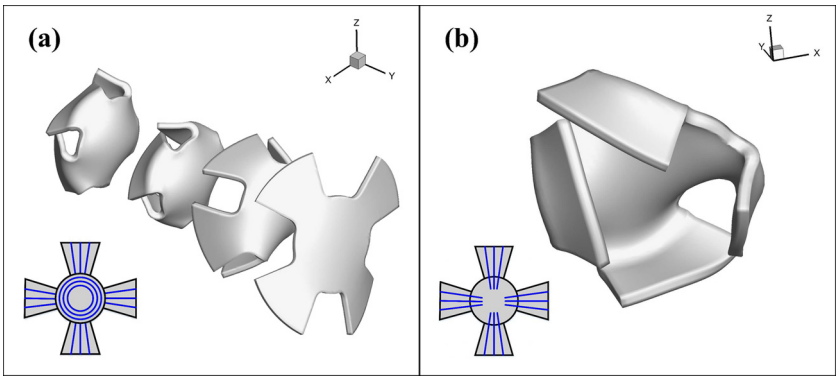

Fig. 15. Comparison of the dynamics of soft robotic baby-jellyfish by distributing active contractions (marked by the blue lines) on (a) arms (i.e., radially) and partial of the circular disk (i.e., azimuthally), and (b) arms only. The four sequential snapshots in (a) highlight a stable directional locomotion in one actuation period. The snapshot in (b) shows an example of unstable asymmetric deformations without applying the azimuthal contraction in the disk to stabilize the structure.

baby jellyfish cannot generate a directional locomotion due to very unstable deformations as shown by the snapshot. We have also tried varying the size of the area covered by radial actuation but without success (not reported here).

While we only consider some simple designs, the FD/active strain model can be generally applied to manipulate elastic structures of arbitrary shapes and sizes. In particular, it is intriguing to incorporate more elaborate constitutive models (e.g., viscoelastic or composite materials) in order to mimick the behaviors of real biological tissues. Moreover, the active strain model can be flexibly implemented in other computational frameworks, either using boundary conforming methods or Cartesian grid methods, to handle coupling of soft actuation and the induced fluid motion. Last but not least, in order to optimize soft robotic systems with a large number of parameters (e.g., shape, stiffness, and actuation distribution) and possibly multiple design objectives (e.g., swimming speed, power, and efficiency), it is desirable to couple the existing CFD tools with multi-objective evolutionary algorithms and packages such as the Unified Non-dominated Sorting Genetic Algorithm (U-NSGA) II/III [71–74]. The integrated framework like this will facilitate design of high-performance soft robotic machines for a wide range of applications in engineering and applied sciences.

Acknowledgements

T.G. acknowledges NSF grant No. CBET-1702987 and MSU's Strategic Partnership Grant. Z.Y. acknowledges the support from the National Natural Science Foundation of China grant No. 91752117.

Appendix A. Supplementary material

Supplementary material related to this article can be found online at https://doi.org/10.1016/j.jcp.2018.10.015.

References

[1] N. Bartlett, M. Tolley, J. Overvelde, J. Weaver, B. Mosadegh, K. Bertoldi, G. Whitesides, R. Wood, A 3d-printed, functionally graded soft robot powered by combustion, Science 349 (2015) 161–165.
[2] C. Majidi, Soft robotics: a perspective–current trends and prospects for the future, Soft Robotics 1 (2014) 5–11.
[3] D. Rus, M. Tolley, Design, fabrication and control of soft robots, Nature 521 (2015) 467–475.
[4] D. Drotman, S. Jadhav, M. Karimi, M. Tolley, et al., 3d printed soft actuators for a legged robot capable of navigating unstructured terrain, in: IEEE International Conference on Robotics and Automation (ICRA 2017), IEEE, 2017, pp. 5532–5538.
[5] J. Nawroth, H. Lee, A. Feinberg, C. Ripplinger, M. McCain, A. Grosberg, J. Dabiri, K. Parker, A tissue-engineered jellyfish with biomimetic propulsion, Nat. Biotechnol. 30 (2012) 792–797.
[6] M. Al-Rubaiai, T. Pinto, D. Torres, N. Sepulveda, X. Tan, Characterization of a 3d-printed conductive pla material with electrically controlled stiffness, in: ASME 2017 Conference on Smart Materials, Adaptive Structures and Intelligent Systems, American Society of Mechanical Engineers, 2017, V001T01A003.
[7] J. Case, E. White, R. Kramer, Sensor enabled closed-loop bending control of soft beams, Smart Mater. Struct. 25 (4) (2016) 045018.
[8] S. Kim, J. Lee, S. An, M. Cho, K. Cho, A large-stroke shape memory alloy spring actuator using double-coil configuration, Smart Mater. Struct. 24 (9) (2015) 095014.
[9] V. Palmre, J. Hubbard, M. Fleming, D. Pugal, S. Kim, K. Kim, K. Leang, An ipmc-enabled bio-inspired bending/twisting fin for underwater applications, Smart Mater. Struct. 22 (1) (2012) 014003.
[10] W. Shan, S. Diller, A. Tutcuoglu, C. Majidi, Rigidity-tuning conductive elastomer, Smart Mater. Struct. 24 (6) (2015) 065001.
[11] S. Trabia, Z. Olsen, K. Kim, Searching for a new ionomer for 3d printable ionic polymer–metal composites: aquivion as a candidate, Smart Mater. Struct. 26 (11) (2017) 115029.
[12] M. Lighthill, Note on the swimming of slender fish, J. Fluid Mech. 9 (1960) 305–317.
[13] E. Purcell, Life at low Reynolds number, Am. J. Phys. 45 (1977) 3–11.
[14] L. Ristroph, S. Childress, Stable hovering of a jellyfish-like flying machine, J. R. Soc. Interface 11 (2014) 20130992.

[15] F. Fang, K. Ho, L. Ristroph, M. Shelley, A computational model of the flight dynamics and aerodynamics of a jellyfish-like flying machine, J. Fluid Mech. 819 (2017) 621.
[16] H. Hu, M. Zhu, N. Patankar, Direct numerical simulations of fluid solid systems using the arbitrary Lagrangian Eulerian technique, J. Comput. Phys. 169 (2001) 427–462.
[17] T. Gao, H. Hu, Deformation of elastic particles in viscous shear flow, J. Comput. Phys. 228 (2009) 2132–2151.
[18] A. Masud, T. Hughes, A space–time Galerkin/least-squares finite element formulation of the Navier–Stokes equations for moving domain problems, Comput. Methods Appl. Mech. Eng. 146 (1997) 91–126.
[19] V. Kalro, T. Tezduyar, A parallel 3d computational method for fluid–structure interactions in parachute systems, Comput. Methods Appl. Mech. Eng. 190 (2000) 321.
[20] P. Le Tallec, J. Mouro, Fluid structure interaction with large structural displacements, Comput. Methods Appl. Mech. Eng. 190 (2001) 3039–3067.
[21] J. Kim, D. Kim, H. Choi, An immersed-boundary finite-volume method for simulations of flow in complex geometries, J. Comput. Phys. 171 (2001) 132–150.
[22] C. Peskin, The immersed boundary method, Acta Numer. 10 (2002) 479–517.
[23] R. Mittal, G. Iaccarino, Immersed boundary methods, Annu. Rev. Fluid Mech. 37 (2005) 239–261.
[24] R. Mittal, H. Dong, M. Bozkurttas, F. Najjar, A. Vargas, A. von Loebbecke, A versatile sharp interface immersed boundary method for incompressible flows with complex boundaries, J. Comput. Phys. 227 (10) (2008) 4825–4852.
[25] R. Bhardwaj, R. Mittal, Benchmarking a coupled immersed-boundary-finite-element solver for large-scale flow-induced deformation, AIAA J. 50 (2011) 1638–1642.
[26] F. Tian, H. Dai, H. Luo, J. Doyle, B. Rousseau, Fluid–structure interaction involving large deformations: 3d simulations and applications to biological systems, J. Comput. Phys. 258 (2014) 451–469.
[27] C. Antoci, M. Gallati, S. Sibilla, Numerical simulation of fluid–structure interaction by sph, Comput. Struct. 85 (2007) 879–890.
[28] X. He, L. Luo, Lattice Boltzmann model for the incompressible Navier–Stokes equation, J. Stat. Phys. 88 (1997) 927.
[29] S. Chen, G. Doolen, Lattice Boltzmann method for fluid flows, Annu. Rev. Fluid Mech. 30 (1998) 329.
[30] T. Gao, Y. Tseng, X. Lu, An improved hybrid Cartesian/immersed boundary method for fluid–solid flows, Int. J. Numer. Methods Fluids 55 (2007) 1189–1211.
[31] H. Huang, X. Lu, An ellipsoidal particle in tube Poiseuille flow, J. Fluid Mech. 822 (2017) 664–688.
[32] H. Huang, X. Yang, X. Lu, Sedimentation of an ellipsoidal particle in narrow tubes, Phys. Fluids 26 (5) (2014) 053302.
[33] S. Park, M. Gazzola, K. Park, S. Park, V. Di Santo, E. Blevins, J. Lind, P. Campbell, S. Dauth, A. Capulli, F. Pasqualini, S. Ahn, A. Cho, H. Yuan, B. Maoz, R. Vijaykumar, J. Choi, K. Deisseroth, G. Lauder, L. Mahadevan, K. Parker, Phototactic guidance of a tissue-engineered soft-robotic ray, Science 353 (2016) 158–162.
[34] Z. Yu, A DLM/FD method for fluid/flexible-body interactions, J. Comput. Phys. 207 (2005) 1–27.
[35] Z. Yu, Y. Wang, X. Shao, Numerical simulation of the flapping of a three-dimensional flexible plate in uniform flow, J. Sound Vib. 331 (2012) 4448–4463.
[36] E. Lee, D. Liu, Finite-strain elastic-plastic theory particularly for plane wave analysis, J. Appl. Phys. 38 (1967) 19–27.
[37] E. Lee, Elastic-plastic deformation at finite strains, J. Appl. Mech. 36 (1969) 1–6.
[38] D. Ambrosi, S. Pezzuto, Active stress vs. active strain in mechanobiology: constitutive issues, J. Elast. 107 (2012) 199.
[39] S. Chester, L. Anand, A coupled theory of fluid permeation and large deformations for elastomeric materials, J. Mech. Phys. Solids 58 (2010) 1879–1906.
[40] H. Tian, Z. Wang, Y. Chen, J. Shao, T. Gao, S. Cai, Polydopamine-coated main-chain liquid crystal elastomer as optically driven artificial muscle, ACS Appl. Mater. Interfaces 10 (2018) 8307–8316.
[41] Z. Suo, Theory of dielectric elastomers, Acta Mech. Solida Sin. 23 (2010) 549–578.
[42] L. Fauci, A. McDonald, Sperm motility in the presence of boundaries, Bull. Math. Biol. 57 (1995) 670–699.
[43] J. Teran, L. Fauci, M. Shelley, Viscoelastic fluid response can increase the speed and efficiency of a free swimmer, Phys. Rev. Lett. 104 (2010) 038101.
[44] R. Glowinski, T. Pan, T. Hesla, D. Joseph, A distributed Lagrange multiplier/fictitious domain method for particulate flows, Int. J. Multiph. Flow 25 (1999) 755–794.
[45] L. Li, S. Sherwin, P. Bearman, A moving frame of reference algorithm for fluid/structure interaction of rotating and translating bodies, Int. J. Numer. Methods Fluids 38 (2002) 187–206.
[46] Z. Yu, X. Shao, A direct-forcing fictitious domain method for particulate flows, J. Comput. Phys. 227 (2007) 292–314.
[47] Z. Yu, X. Shao, A three-dimensional fictitious domain method for the simulation of fluid–structure interactions, J. Hydrodyn. B 22 (5) (2010) 178–183.
[48] S. Turek, J. Hron, Proposal for numerical benchmarking of fluid–structure interaction between an elastic object and laminar incompressible flow, in: Fluid–Structure Interaction, Springer, 2006, pp. 371–385.
[49] W. Huang, H. Sung, Three-dimensional simulation of a flapping flag in a uniform flow, J. Fluid Mech. 653 (2010) 301–336.
[50] X. Yang, X. Zhang, Z. Li, G. He, A smoothing technique for discrete delta functions with application to immersed boundary method in moving boundary simulations, J. Comput. Phys. 228 (20) (2009) 7821–7836.
[51] C. Hamlet, L. Fauci, E. Tytell, The effect of intrinsic muscular nonlinearities on the energetics of locomotion in a computational model of an anguilliform swimmer, J. Theor. Biol. 385 (2015) 119.
[52] E. Tytell, M. Leftwich, C. Hsu, B. Griffith, A. Cohen, A. Smits, C. Hamlet, L. Fauci, Role of body stiffness in undulatory swimming: insights from robotic and computational models, Phys. Rev. Fluids 1 (2016) 073202.
[53] T. Williams, G. Bowtell, N. Curtin, Predicting force generation by lamprey muscle during applied sinusoidal movement using a simple dynamic model, J. Exp. Biol. 201 (1998) 869.
[54] R. Ogden, Nonlinear Elastic Deformations, Dover, 1984.
[55] W. van Rees, M. Gazzola, P. Koumoutsakos, Optimal morphokinematics for undulatory swimmers at intermediate Reynolds numbers, J. Fluid Mech. 775 (2015) 178–188.
[56] J. Zhou, R. Adrian, S. Balachandar, T. Kendall, Mechanisms for generating coherent packets of hairpin vortices in channel flow, J. Fluid Mech. 387 (1999) 353–396.
[57] Q. Chen, Q. Zhong, M. Qi, X. Wang, Comparison of vortex identification criteria for planar velocity fields in wall turbulence, Phys. Fluids 27 (8) (2015) 085101.
[58] J. Wu, H. Ma, M. Zhou, Vorticity and Vortex Dynamics, Springer, 2006.
[59] M. Sahin, K. Mohseni, An arbitrary Lagrangian–Eulerian formulation for the numerical simulation of flow patterns generated by the hydromedusa aequorea Victoria, J. Comput. Phys. 228 (2009) 4588.
[60] G. Hersch, L. Miller, Reynolds number limits for jet propulsion: a numerical study of simplified jellyfish, J. Theor. Biol. 285 (2011) 84.
[61] S. Alben, L. Miller, J. Peng, Efficient kinematics for jet-propelled swimming, J. Fluid Mech. 733 (2013) 100.
[62] S. Park, C. Chang, W. Huang, H. Sung, Simulation of swimming oblate jellyfish with a paddling-based locomotion, J. Fluid Mech. 748 (2014) 731.
[63] M. Sahin, K. Mohseni, S. Colin, The numerical comparison of flow patterns and propulsive performances for the hydromedusae sarsia tubulosa and aequorea Victoria, J. Exp. Biol. 212 (2009) 2656.
[64] S. Park, B. Kim, J. Lee, W. Huang, H. Sung, Dynamics of prolate jellyfish with a jet-based locomotion, J. Fluids Struct. 57 (2015) 331.

[65] C. Gambini, B. Abou, A. Ponton, A.J.M. Cornelissen, Micro- and macrorheology of jellyfish extracellular matrix, Biophys. J. 102 (2012) 1–9.
[66] S. Colin, J. Costello, Morphology, swimming performance and propulsive mode of six co-occurring hydromedusae, J. Exp. Biol. 205 (2002) 427.
[67] S. Colin, J. Costello, E. Klos, In situ swimming and feeding behavior of eight co-occurring hydromedusae, Mar. Ecol. Prog. Ser. 253 (2003) 305.
[68] J. Costello, S. Colin, J. Dabiri, Medusan morphospace: phylogenetic constraints, biomechanical solutions, and ecological consequences, Invertebr. Biol. 127 (2008) 265.
[69] J. Dabiri, S. Colin, J. Costello, M. Gharib, Flow patterns generated by oblate medusan jellyfish: field measurements and laboratory analyses, J. Exp. Biol. 208 (2005) 1257.
[70] J. Dabiri, S. Colin, K. Katija, J. Costello, A wake-based correlate of swimming performance and foraging behavior in seven co-occurring jellyfish species, J. Exp. Biol. 213 (2010) 1217.
[71] K. Deb, A. Pratap, S. Agarwal, T. Meyarivan, A fast and elitist multiobjective genetic algorithm: Nsga-ii, IEEE Trans. Evol. Comput. 6 (2002) 182–197.
[72] H. Seada, K. Deb, A unified evolutionary optimization procedure for single, multiple, and many objectives, IEEE Trans. Evol. Comput. 20 (2016) 358.
[73] K. Deb, H. Jain, An evolutionary many-objective optimization algorithm using reference-point-based nondominated sorting approach, part I: solving problems with box constraints, IEEE Trans. Evol. Comput. 18 (2014) 577–601.
[74] H. Jain, K. Deb, An evolutionary many-objective optimization algorithm using reference-point-based nondominated sorting approach, part II: handling constraints and extending to an adaptive approach, IEEE Trans. Evol. Comput. 18 (2014) 602–622.
[75] A. Hoover, B. Griffith, L. Miller, Quantifying performance in the medusan mechanospace with an actively swimming three-dimensional jellyfish model, J. Fluid Mech. 813 (2017) 1112–1155.